



# Understanding the effect of synthesis temperature on the structural and electrochemical characteristics of layered-spinel composite cathodes for lithium-ion batteries

Eun-Sung Lee<sup>a</sup>, Ashfia Huq<sup>b</sup>, Arumugam Manthiram<sup>a,\*</sup>

<sup>a</sup> Materials Science and Engineering Program & Texas Materials Institute, The University of Texas at Austin, Austin, TX 78712, USA

<sup>b</sup> Chemical and Engineering Materials Division, Neutron Sciences Directorate, Oak Ridge National Laboratory, Oak Ridge, TN 37831, USA

## HIGHLIGHTS

- The synthesis temperature affects characteristics of the layered-spinel composites.
- Chemical compositions and weight percentages of composite cathodes are refined.
- Cation ordering of the spinel phase increases with decreasing synthesis temperature.
- The capacity of the layered phase increases with decreasing synthesis temperature.

## ARTICLE INFO

### Article history:

Received 29 December 2012

Received in revised form

30 March 2013

Accepted 1 April 2013

Available online 10 April 2013

### Keywords:

Lithium-ion batteries

Layered-spinel composite cathodes

Structural analysis

Cation ordering

## ABSTRACT

The effect of synthesis temperature on the structural and electrochemical characteristics of the layered-spinel composite cathode system  $x\text{Li}[\text{Li}_{0.2}\text{Mn}_{0.6}\text{Ni}_{0.2}]\text{O}_2-(1-x)\text{Li}[\text{Mn}_{1.5}\text{Ni}_{0.5}]\text{O}_4$  ( $0 \leq x \leq 1$ ) has been investigated. With a joint neutron diffraction (ND) and X-ray diffraction (XRD) Rietveld refinement method, the composition and weight percent variations of the layered and spinel phases in this composite cathode system have been obtained as a function of  $x$  and synthesis temperature. While no significant composition and weight percent variations are found with the synthesis temperature, the electrochemical characteristics of both the layered and spinel phases in the composites are significantly affected by the synthesis temperature. In contrast to the layered sample ( $x = 1$ ), the capacity of the layered phase in the composites increases with decreasing synthesis temperature due to an increase in surface area. Conversely, the effect of synthesis temperature on the spinel phase is similar in both the spinel sample ( $x = 0$ ) and the composite samples. However, the lower synthesis temperature increases the cation ordering in the 16d octahedral sites of the spinel phase, which changes the voltage profiles below 3 V due to the decrease in the lattice distortion during lithium ion insertion into the empty 16c octahedral sites.

© 2013 Elsevier B.V. All rights reserved.

## 1. Introduction

Lithium-ion batteries are the most promising rechargeable battery system for both vehicle applications and stationary storage of electricity produced by renewables like solar and wind energies as they offer much higher energy density than other rechargeable systems. Unfortunately, the current lithium-ion technology does not fully meet the requirement of these applications in terms of energy and power densities [1,2]. In order to increase both the energy and power, new cathode materials with higher capacity or

higher operating voltage need to be developed [3]. In this regard, the high-capacity layered  $\text{Li}[\text{Li},\text{Mn},\text{Ni},\text{Co}]\text{O}_2$  and the high-voltage (5 V) spinel  $\text{LiMn}_{1.5}\text{Ni}_{0.5}\text{O}_4$  are promising, respectively, due to their high energy density and high power density [2,3]. The lithium-rich layered  $\text{Li}[\text{Li},\text{Mn},\text{Ni},\text{Co}]\text{O}_2$  oxides exhibit capacities of  $\sim 250 \text{ mAh g}^{-1}$  when charged above 4.5 V [4–6], but suffer from inferior rate capability and low first cycle coulombic efficiency. On the other hand, the  $\text{LiMn}_{1.5}\text{Ni}_{0.5}\text{O}_4$  spinel exhibits high power capability due to the three-dimensional diffusion of lithium ions with an operating voltage of  $\sim 4.7$  [7,8], but suffers from its limited capacity ( $\sim 130 \text{ mAh g}^{-1}$ ) above 3 V. Integrating the lithium-rich layered and the high-voltage spinel oxides into a composite cathode could give a combination of high energy and power. Furthermore, as both the layered and spinel oxides are based on a cubic

\* Corresponding author. Tel.: +1 512 471 1791; fax: +1 512 471 7681.

E-mail address: [rmanth@mail.utexas.edu](mailto:rmanth@mail.utexas.edu) (A. Manthiram).

close packed oxygen array, the composite can be expected to have good interfacial compatibility.

Accordingly, two layered-spinel composite systems,  $x\text{Li}_2\text{MnO}_3-(1-x)\text{Li}_{1+\delta}\text{Mn}_{2-\delta}\text{O}_4$  ( $0 \leq \delta \leq 1/3$ ) [9,10] and  $x(\text{Li}_2\text{MnO}_3 \cdot \text{Li}[\text{Mn}_{0.5}\text{Ni}_{0.5}]\text{O}_2)-(1-x)\text{Li}[\text{Mn}_{1.5}\text{Ni}_{0.5}]\text{O}_4$  ( $0 \leq x \leq 1$ ) [11–14] have been studied in the literature. The performances of these layered-spinel composites exceed those of the individual layered or spinel oxides in terms of both specific capacity and cycle performance when cycled between 5 and 2 V at low current rates. In order to understand the structural complexity of the layered-spinel composite materials, various techniques such as X-ray diffraction (XRD), X-ray absorption spectroscopy (XAS), and nuclear magnetic resonance (NMR) have been used both for the pristine state and during first cycle [10,12]. Although the electrochemical activities of the layered and spinel phases were confirmed with these techniques, the compositional variations of the layered and spinel phases in the composite samples could not be obtained; because of the same basic cubic close packed oxygen array, the actual composition and content of the layered and spinel phases in the composite could be different from the nominal composition and content. We reported recently the compositional and wt. % variations of the layered and spinel phases for the system  $x\text{Li}[\text{Li}_{0.2}\text{Mn}_{0.6}\text{Ni}_{0.17}\text{Co}_{0.03}]\text{O}_2-(1-x)\text{Li}[\text{Mn}_{1.5}\text{Ni}_{0.425}\text{Co}_{0.075}]\text{O}_4$  ( $0 \leq x \leq 1$ ) by employing a joint XRD and neutron diffraction (ND) Rietveld refinement method [15]. The investigation provided useful information for explaining the unique structural and electrochemical characteristics of the layered-spinel composite materials during extended cycling.

However, the previous study was on samples synthesized at a specific temperature (800 °C). Considering the cubic close-packed array in both the layered and spinel, the synthesis temperatures could have a significant influence on the composition and amount of the layered and spinel phases in the composite. Accordingly, we present here an investigation of the effect of synthesis temperature on the structural and electrochemical characteristics of the layered-spinel composite system  $x\text{Li}[\text{Li}_{0.2}\text{Mn}_{0.6}\text{Ni}_{0.2}]\text{O}_2-(1-x)\text{Li}[\text{Mn}_{1.5}\text{Ni}_{0.5}]\text{O}_4$  ( $0 \leq x \leq 1$ ), employing XRD, ND, and electrochemical analysis. In this system, the nominal oxidation states of manganese and nickel are, respectively, 4+ and 2+, and the Mn/Ni ratio are 3:1 in both the layered and spinel phases.

## 2. Experimental

### 2.1. Synthesis

Five  $x\text{Li}[\text{Li}_{0.2}\text{Mn}_{0.6}\text{Ni}_{0.2}]\text{O}_2-(1-x)\text{Li}[\text{Mn}_{1.5}\text{Ni}_{0.5}]\text{O}_4$  samples with  $x = 0, 0.25, 0.5, 0.75$ , and 1.0 as indicated in Fig. 1 were prepared by mechanically mixing the required amount of mixed metal

hydroxides (Mn:Ni = 3:1) with lithium hydroxide, followed by firing at 700, 800, and 900 °C for 6 h in air and cooling at 5 °C min<sup>-1</sup>. The mixed metal hydroxides were synthesized by a co-precipitation method, as described previously [15], involving a drop-wise addition of a required amount of the aqueous metal acetate (Mn:Ni = 3:1) solution into a 2 M KOH solution under continuous stirring. The Li:Mn + Ni metal molar ratio in the mixtures were 0.5, 0.62, 0.79, 1.05, and 1.5, respectively, to obtain the  $x = 0, 0.25, 0.5, 0.75$ , and 1 samples in the  $x\text{Li}[\text{Li}_{0.2}\text{Mn}_{0.6}\text{Ni}_{0.2}]\text{O}_2-(1-x)\text{Li}[\text{Mn}_{1.5}\text{Ni}_{0.5}]\text{O}_4$  system.

### 2.2. Characterization

The lithium and transition metal contents in the synthesized samples were analyzed with a Varian 715-ES inductively coupled plasma-atomic emission spectrometer (ICP-AES). ND data were obtained with the general purpose powder diffraction beamline POWGEN at the Spallation Neutron Source [16]. ND data were collected at room-temperature with wavelengths of 1.066 and 2.665 Å, which cover a d spacing range of 0.3–6.2 Å. XRD data were collected with a Rigaku Ultima-IV system (Cu K $\alpha$  radiation). XRD and ND joint Rietveld refinements with the software package GSAS and EXPGUI interface [17,18] were used to characterize the structure of representative pristine samples. The lattice parameters of each phase in other pristine samples were obtained with the Rigaku PDXL commercial software [19]. Fourier transform infrared (FTIR) spectroscopy data were obtained with KBr pellets with a PerkinElmer IR spectrometer. Multi-point Brunauer–Emmett–Teller (BET) surface area data were collected with an automatic nitrogen gas absorption analyzer (NOVA 2000, Quantachrome) using physical adsorption at 77 K.

Electrochemical properties of the synthesized composite samples were evaluated with 2032-type coin cells with lithium metal as a counter electrode. The cathodes consisted of a mixture of 80 wt. % active material, 10 wt. % Super P conductive carbon additive, and 10 wt. % polyvinylidene fluoride (PVDF) binder. Coin cells were assembled in an Ar-filled glove box with 1 M LiPF<sub>6</sub> in ethylene carbonate (EC)/diethyl carbonate (DEC) (1:1 v/v) as the electrolyte and Celgard polypropylene as the separator. All electrochemical tests were performed between 2 and 5 V vs. Li/Li<sup>+</sup> at a current density of 10 mA g<sup>-1</sup> (~C/25 rate assuming a capacity of ~250 mAh g<sup>-1</sup>). For the *ex situ* XRD analysis, cathodes were removed from the coin cells in an Ar-filled glove box after the intended number of cycles was completed and the cells were in a discharged state. The cathodes were dried at room temperature and attached to a Kapton film before exposure to air.

## 3. Results and discussion

### 3.1. Chemical and structural analysis

ICP-AES analysis data of the metal ion contents in the  $x\text{Li}[\text{Li}_{0.2}\text{Mn}_{0.6}\text{Ni}_{0.2}]\text{O}_2-(1-x)\text{Li}[\text{Mn}_{1.5}\text{Ni}_{0.5}]\text{O}_4$  composite materials synthesized with different temperatures are given in Table 1. The experimental Mn/Ni and Li/[Mn + Ni] molar ratios are in good agreement with the designed nominal values, considering the experimental errors with ICP.

Fig. 2 shows the XRD and ND patterns of the pristine  $x\text{Li}[\text{Li}_{0.2}\text{Mn}_{0.6}\text{Ni}_{0.2}]\text{O}_2-(1-x)\text{Li}[\text{Mn}_{1.5}\text{Ni}_{0.5}]\text{O}_4$  ( $x = 0, 0.25, 0.5, 0.75$ , and 1) composite materials prepared at 800 °C. The  $x = 0.25, 0.5$ , and 0.75 samples show reflections from both the layered (*C2/m*) and spinel (*Fd-3m*) phases in the XRD and ND patterns. The relative intensities of the reflections from the layered phase increase with increasing  $x$ , as expected. As reported before [15], the composite materials show much clear and stronger superstructure reflections

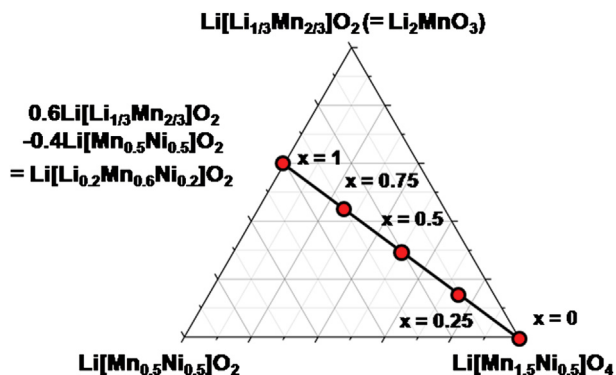


Fig. 1. Compositional phase diagram of the  $x\text{Li}[\text{Li}_{0.2}\text{Mn}_{0.6}\text{Ni}_{0.2}]\text{O}_2-(1-x)\text{Li}[\text{Mn}_{1.5}\text{Ni}_{0.5}]\text{O}_4$  layered-spinel composite system.

**Table 1**

ICP-AES compositional analysis data of the  $x\text{Li}[\text{Li}_{0.2}\text{Mn}_{0.6}\text{Ni}_{0.2}]\text{O}_2-(1-x)\text{Li}[\text{Mn}_{1.5}\text{Ni}_{0.5}]\text{O}_4$  composite materials.

x	Synthesis temperature	Mn/Ni ratio	Li/[Mn + Ni] ratio	
			Nominal	Experimental
0	700 °C	3.0	0.50	0.52
	800 °C	3.1		0.53
	900 °C	3.1		0.51
0.25	700 °C	3.1	0.62	0.65
	800 °C	3.1		0.60
	900 °C	3.1		0.62
0.5	700 °C	3.1	0.79	0.79
	800 °C	3.1		0.79
	900 °C	3.1		0.78
0.75	700 °C	3.1	1.05	1.07
	800 °C	3.1		1.07
	900 °C	3.1		1.05
1	700 °C	3.1	1.50	1.55
	800 °C	3.1		1.53
	900 °C	3.1		1.49

in the  $2\theta$  range of 20.5–22.5° due to the higher occupancy of lithium ions in the transition metal layer than that based on the nominal composition [20,21]. Notably, the intensities of the reflections and hence the phase fraction of the cubic impurity phase are much higher than that observed with the cobalt-doped composite materials in our previous study [15], indicating that the presence of Co restricts the formation of this impurity phase. Similar X-ray scattering factors of Mn, Ni and the low X-ray scattering factor of Li make it hard to refine the occupancy of the atoms in each phase with XRD data alone. However, the occupancy of each atom could be refined in each phase by combining the XRD and ND data as Li, Mn, and Ni have significantly different ND scattering factors.

In order to compare the structural and compositional changes of the pristine  $x\text{Li}[\text{Li}_{0.2}\text{Mn}_{0.6}\text{Ni}_{0.2}]\text{O}_2-(1-x)\text{Li}[\text{Mn}_{1.5}\text{Ni}_{0.5}]\text{O}_4$  ( $x = 0, 0.25, 0.5, 0.75$ , and 1) composite materials, chemical compositions and weight percentages of each phase are refined for the five pristine samples synthesized at 800 °C and the results are summarized in Table 2. During the refinement process, the site occupancy of lithium and oxygen in the spinel phase and oxygen in the layered phase are fixed to 1. The nominal compositions are applied

**Table 2**

Refined chemical compositions and weight percentages of the layered, spinel, and cubic impurity phases in the  $x\text{Li}[\text{Li}_{0.2}\text{Mn}_{0.6}\text{Ni}_{0.2}]\text{O}_2-(1-x)\text{Li}[\text{Mn}_{1.5}\text{Ni}_{0.5}]\text{O}_4$  composite materials synthesized at 800 °C.

x	Chemical composition			Weight %			Li/[Mn + Ni] ratio
	Atom	Spinel (Fd-3m)	Layered (C2/m)	Spinel (Fd-3m)	Layered (C2/m)	Cubic impurity	
0	Li	1	1.20	91.5	4.5	3.9	0.52
	Mn	1.566(1)	0.60				
	Ni	0.434(1)	0.20				
0.25	Li	1	1.36(4)	74.7	13.9	11.4	0.65
	Mn	1.557(1)	0.62(3)				
	Ni	0.443(1)	0.02(1)				
0.50	Li	1	1.31(2)	59.8	33.2	7.0	0.85
	Mn	1.549(1)	0.65(1)				
	Ni	0.452(1)	0.04(1)				
0.75	Li	1	1.29(1)	29.4	60.6	10.0	1.16
	Mn	1.540(2)	0.65(1)				
	Ni	0.460(1)	0.06(1)				
1.00	Li	1	1.27(1)	8.5	91.5		1.62
	Mn	1.5	0.59(1)				
	Ni	0.5	0.14(1)				

for the layered phase in the  $x = 0$  sample and spinel phase in the  $x = 1$  sample as little or a small fraction of them is expected to be present in those samples. In the  $x = 0$  sample, small fractions of layered (~4.5 wt. %) and cubic impurity phases (~3.9 wt. %) are detected. Even though previous studies indexed this cubic impurity phase as a rocksalt-type  $\text{Li}_y\text{Ni}_{1-y}\text{O}$  phase that has a lattice parameter of ~4.2 Å [8,12,22], we indexed this cubic impurity phase as the  $\text{Ni}_6\text{MnO}_8$  phase [15,23], which has a lattice parameter of ~8.3 Å, because the peak at 4.14 Å in the ND pattern (See Supporting information Figure S1) could not exist if the cubic impurity phase has a lattice parameter of ~4.2 Å. Due to the presence of the  $\text{Ni}_6\text{MnO}_8$  impurity phase, the Ni content in the spinel phase appears to be lower than the nominal composition. In the  $x = 1$  sample, a small fraction (~8.5 wt. %) of the spinel phase is observed, which leads to an increase in the lithium content in the layered phase compared to the nominal value. For the composite samples ( $x = 0.25, 0.5$ , and  $0.75$ ), a relatively large wt. % (7.0–11.4%) of  $\text{Ni}_6\text{MnO}_8$  cubic impurity phases are observed as expected in the XRD and ND data in Fig. 2. The presence of the  $\text{Ni}_6\text{MnO}_8$  cubic

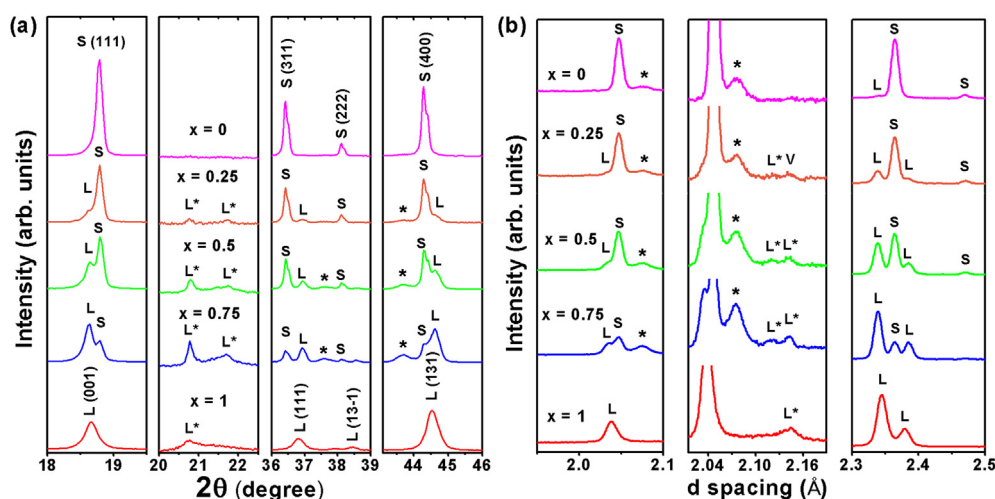


**Fig. 2.** Selected portions of the (a) XRD and (b) ND patterns of the  $x\text{Li}[\text{Li}_{0.2}\text{Mn}_{0.6}\text{Ni}_{0.2}]\text{O}_2-(1-x)\text{Li}[\text{Mn}_{1.5}\text{Ni}_{0.5}]\text{O}_4$  ( $x = 0, 0.25, 0.5, 0.75$ , and 1) samples synthesized at 800 °C to show the various phases present. S and L refer, respectively, to the cubic spinel and layered phases.  $L^*$  refers to the superstructure reflections arising from an ordering among the  $\text{Li}^+$ ,  $\text{Mn}^{4+}$ , and  $\text{Ni}^{2+}$  ions in the layered phase. The asterisk refers to the  $\text{Ni}_6\text{MnO}_8$  cubic impurity phase. V refers to the reflection arising from the vanadium can used for the ND experiments.

impurity phase in the composite samples reduces the nickel content in both the spinel and layered phases. Notably, the Ni content in the layered phase is affected more than that in the spinel phase since the difference between the actual and nominal wt. % of the layered phase is larger than that of the spinel phase. So it increases the lithium and manganese contents above the expected nominal values in the layered phase.

In order to investigate the structural changes of the composite materials with varying synthesis temperatures, XRD patterns of the pristine  $x\text{Li}[\text{Li}_{0.2}\text{Mn}_{0.6}\text{Ni}_{0.2}]\text{O}_2-(1-x)\text{Li}[\text{Mn}_{1.5}\text{Ni}_{0.5}]\text{O}_4$  ( $x = 0, 0.25, 0.5, 0.75, \text{ and } 1$ ) composite materials synthesized at different temperatures are compared in Fig. 3. The obtained lattice parameter values for each phase are summarized in Table 3. Lattice parameters are obtained with the XRD and ND joint refinement for

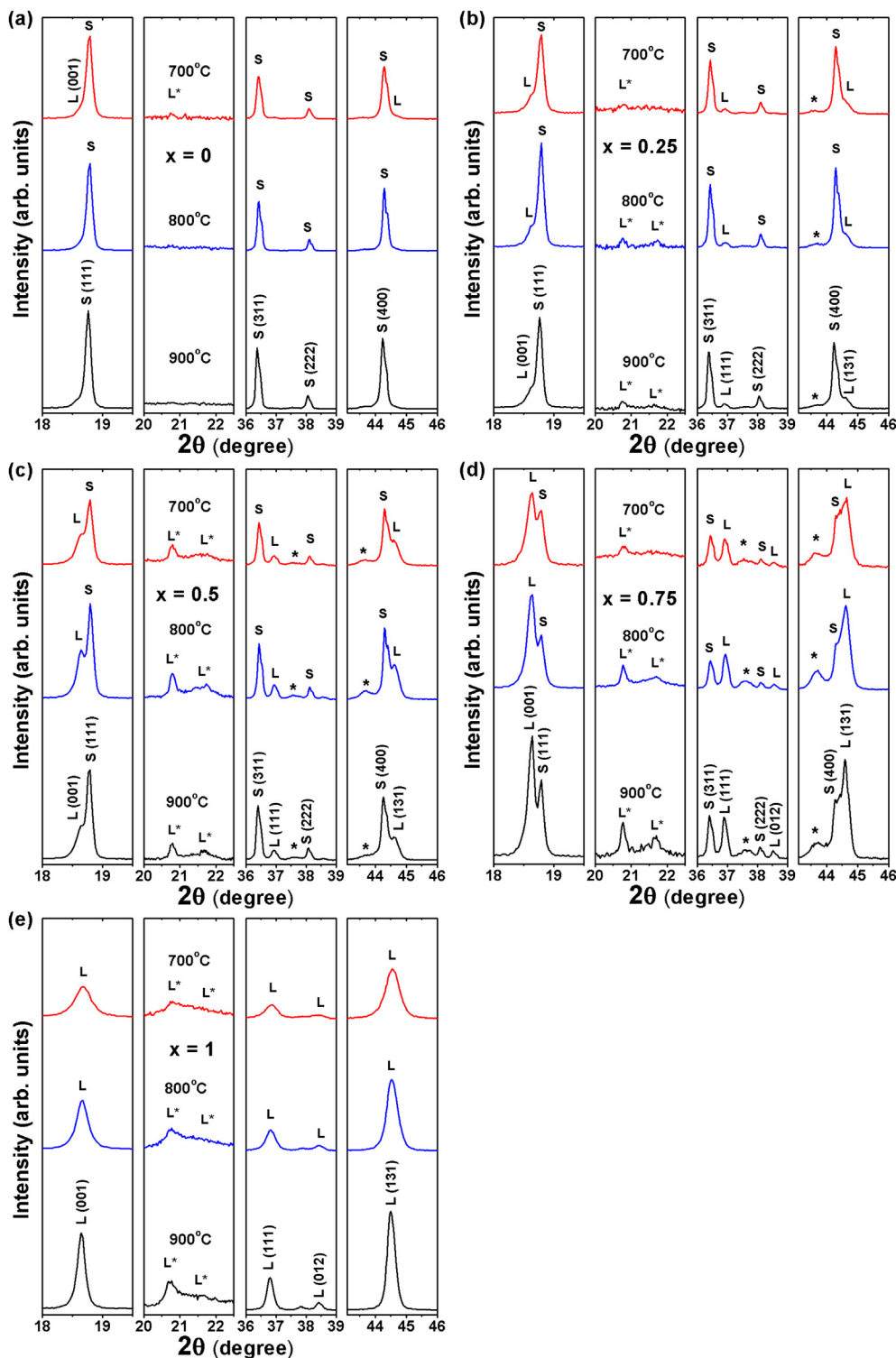


**Fig. 3.** XRD of the  $x\text{Li}[\text{Li}_{0.2}\text{Mn}_{0.6}\text{Ni}_{0.2}]\text{O}_2-(1-x)\text{Li}[\text{Mn}_{1.5}\text{Ni}_{0.5}]\text{O}_4$  samples synthesized at various temperatures: (a)  $x = 0$ , (b)  $x = 0.25$ , (c)  $x = 0.5$ , (d)  $x = 0.75$ , and (e)  $x = 1$ . S and L refer, respectively, to the cubic spinel and layered phases. L\* refers to the superstructure reflections arising from an ordering among the  $\text{Li}^+$ ,  $\text{Mn}^{4+}$ , and  $\text{Ni}^{2+}$  ions in the layered phase. The asterisk refers to the  $\text{NiMn}_6\text{O}_8$  cubic impurity phase.



**Table 3**Lattice parameters of the layered and spinel phases in  $x\text{Li}[\text{Li}_{0.2}\text{Mn}_{0.6}\text{Ni}_{0.2}]\text{O}_2-(1-x)\text{Li}[\text{Mn}_{1.5}\text{Ni}_{0.5}]\text{O}_4$  composite materials synthesized at different temperatures.

$x$	Synthesis Temp.	Spinel ( $Fd-3m$ )		Layered ( $C2/m$ )				
		$a$ (Å)	$V$ (Å <sup>3</sup> )	$a$ (Å)	$b$ (Å)	$c$ (Å)	$\beta$	$V$ (Å <sup>3</sup> )
0	700 °C	8.1731(1)	545.9					
	800 °C	8.1763(1)	546.6					
	900 °C	8.1801(1)	547.4					
0.25	700 °C	8.1718(4)	545.7	4.9322(3)	8.5318(10)	5.0329(3)	109.32(1)	199.9
	800 °C	8.1754(1)	546.4	4.9414(2)	8.5529(3)	5.0447(1)	109.29(1)	201.2
	900 °C	8.1810(3)	547.5	4.9374(2)	8.5448(6)	5.0377(1)	109.32(1)	200.6
0.5	700 °C	8.1724(1)	545.8	4.9372(2)	8.5450(3)	5.0409(1)	109.15(1)	200.8
	800 °C	8.1746(1)	546.3	4.9412(1)	8.5530(1)	5.0441(1)	109.28(1)	201.2
	900 °C	8.1839(1)	548.1	4.9404(1)	8.5496(2)	5.0452(1)	109.30(1)	201.1
0.75	700 °C	8.1706(6)	545.5	4.9419(6)	8.5255(11)	5.0370(5)	109.26(1)	200.3
	800 °C	8.1752(1)	546.4	4.9418(1)	8.5539(1)	5.0443(1)	109.29(1)	201.3
	900 °C	8.1773(2)	546.8	4.9406(6)	8.5522(11)	5.0508(6)	109.26(1)	201.5
1	700 °C			4.9719(9)	8.5540(2)	5.0301(12)	109.23(1)	202.0
	800 °C			4.9591(2)	8.5779(2)	5.0299(1)	109.19(1)	202.1
	900 °C			4.9599(5)	8.5782(9)	5.0359(5)	109.25(1)	202.3

the  $x = 0$  and 0.5 samples synthesized at 700, 800, and 900 °C and for the  $x = 0.25, 0.75$ , and 1 samples synthesized at 800 °C. Lattice parameters of all other samples are obtained with the XRD data due to the limitation in the availability of ND beamtime. The samples of the spinel only composition  $\text{Li}[\text{Mn}_{1.5}\text{Ni}_{0.5}]\text{O}_4$  ( $x = 0$ ) can have two different crystallographic structures depending on the synthesis temperature: samples synthesized at high temperatures ( $>700$  °C) have the disordered phase with the space group  $Fd-3m$ , while synthesis or post annealing at 700 °C stabilizes the ordered phase with a 3:1 ordering of  $\text{Mn}^{4+}$  and  $\text{Ni}^{2+}$  ions in the 12d and 4b octahedral sites, respectively, decreasing the symmetry to the space group  $P4_332$  [24–27]. The superstructure reflections, which originate from the transition metal ordering in the 16d octahedral sites, are not observed in the XRD patterns irrespective of thermal history. The lattice parameter of the cubic spinel phase gradually increases with increasing synthesis temperature due to the (i) decreased solubility of Ni in the spinel lattice and the increased amount of  $\text{Mn}^{3+}$  in the spinel phase at high temperature [28] and (ii) decreased degree of transition metal ordering in 16d octahedral sites [8,29–31]. In the ordered spinel phase ( $P4_332$ ), space optimization is possible because the larger  $\text{Ni}^{2+}$  ions and the smaller  $\text{Mn}^{4+}$  ions occupy, respectively, the larger 4b sites and smaller 12d sites [30]. Therefore, the lattice parameter of the spinel phase increases with decreasing degree of ordering in the 16d sites [32].

Due to the similar X-ray scattering factor of Mn and Ni, XRD is not a powerful method for identification of the transition-metal ordering in the spinel phase. In contrast, the infrared spectra and ND data can be used for identifying transition metal ordering in the spinel phase [24,30,33,34]. In the ordered spinel phase, the infrared spectra has well-distinguished peaks due to the existence of long-range order and the ND pattern has the superstructure reflections from the transition metal ordering in the 16d octahedral sites. The infrared spectra of the  $x = 0$  composition synthesized at different temperatures are compared in Fig. 4(a). The number of distinctive peaks increases with decreasing synthesis temperature, supporting the idea of increased transition metal ordering in the spinel phase. The sample synthesized at 700 °C has seven distinctive bands and the observed wavenumbers match with the values in the literature [24,27]. In addition, we can see in Fig. 4(b) that the ND data of the sample synthesized at 700 °C show superstructure reflections, which originate from the transition metal ordering in the 16d octahedral sites. From the decrease in the refined lattice parameters, existence of superstructure reflections in the ND data, and infrared spectroscopy data, we can conclude that the degree of transition metal ordering in the spinel phase increases with decreasing synthesis temperature. Furthermore, very weak

reflections corresponding to the layered phase are detected both in the XRD and ND patterns of the sample synthesized at 700 °C.

The samples of the layered only composition ( $x = 1$ ) have the layered structure with the space group  $C2/m$  [35]. The peak shape in the XRD patterns gradually becomes broad and asymmetric with decreasing synthesis temperature possibly due to the decreased particle size and increased amount of secondary spinel phase in the sample. The layered phase differs from the pure spinel composition in that the synthesis temperature does not have a noticeable effect on the lattice parameter. For the composite samples ( $x = 0.25, 0.5$ , and 0.75), similar trends of lattice parameter changes are observed for the spinel and layered phases. The lattice parameter of the

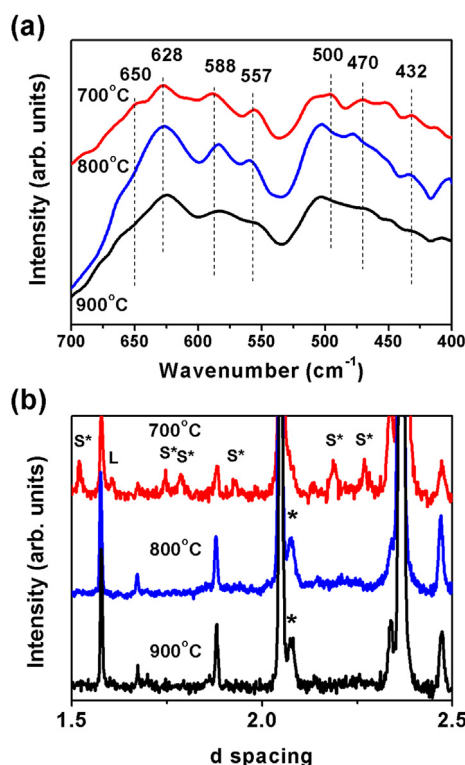


**Fig. 4.** (a) Infrared spectra and (b) ND patterns of the  $x\text{Li}[\text{Li}_{0.2}\text{Mn}_{0.6}\text{Ni}_{0.2}]\text{O}_2-(1-x)\text{Li}[\text{Mn}_{1.5}\text{Ni}_{0.5}]\text{O}_4$  ( $x = 0$ ) samples synthesized at various temperatures.  $S^*$  refers to the superstructure reflections arising from an ordering of the  $\text{Mn}^{4+}$  and  $\text{Ni}^{2+}$  ions in the 16d octahedral sites of the spinel phase. The asterisk refers to the  $\text{NiMn}_2\text{O}_4$  cubic impurity phase.

**Table 4**  
Refined chemical compositions, weight percentages, and surface areas of the  $0.5\text{Li}[\text{Li}_{0.2}\text{Mn}_{0.6}\text{Ni}_{0.2}]\text{O}_2-0.5\text{Li}[\text{Mn}_{1.5}\text{Ni}_{0.5}]\text{O}_4$  composite materials synthesized at different temperatures.

Synthesis temperature	Chemical composition			Weight %			Surface area ( $\text{m}^2 \text{g}^{-1}$ )
	Atom	Spinel ( $Fd-3m$ )	Layered ( $C2/m$ )	Spinel ( $Fd-3m$ )	Layered ( $C2/m$ )	Cubic impurity	
700 °C	Li	1	1.29(2)	55.6	37.2	7.2	2.77
	Mn	1.524(1)	0.66(2)				
	Ni	0.476(1)	0.07(1)				
800 °C	Li	1	1.31(2)	59.8	33.2	7.0	1.21
	Mn	1.549(1)	0.65(1)				
	Ni	0.452(1)	0.04(1)				
900 °C	Li	1	1.26(1)	61.5	31.3	7.0	0.03
	Mn	1.566(1)	0.69(1)				
	Ni	0.434(1)	0.04(1)				

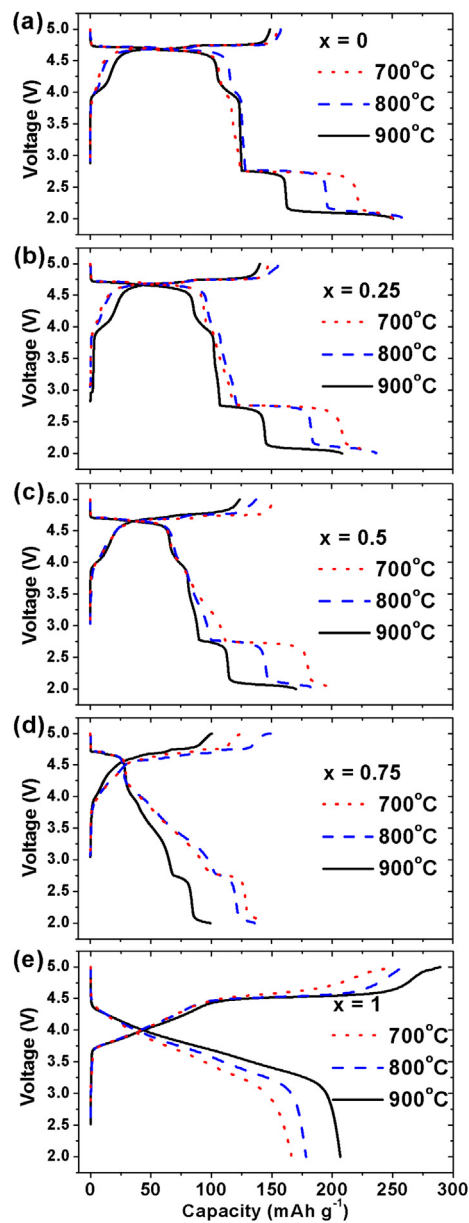


**Fig. 5.** First cycle charge–discharge profiles of the  $x\text{Li}[\text{Li}_{0.2}\text{Mn}_{0.6}\text{Ni}_{0.2}]\text{O}_2-(1-x)\text{Li}[\text{Mn}_{1.5}\text{Ni}_{0.5}]\text{O}_4$  samples synthesized at various temperatures when cycled between 2 and 5 V at  $10 \text{ mA g}^{-1}$ : (a)  $x = 0$ , (b)  $x = 0.25$ , (c)  $x = 0.5$ , (d)  $x = 0.75$ , and (e)  $x = 1$ .

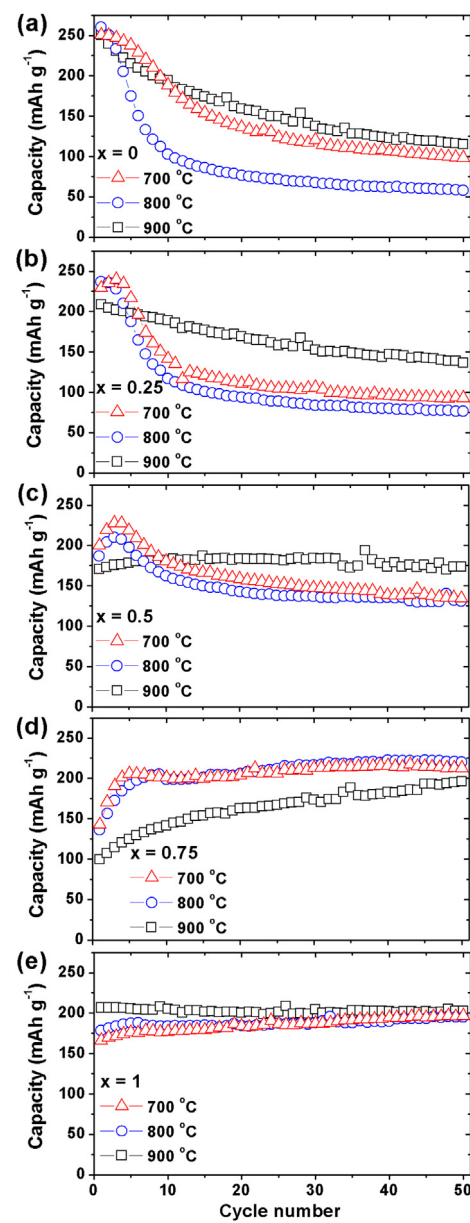


**Fig. 6.** Cycle performance data of the  $x\text{Li}[\text{Li}_{0.2}\text{Mn}_{0.6}\text{Ni}_{0.2}]\text{O}_2-(1-x)\text{Li}[\text{Mn}_{1.5}\text{Ni}_{0.5}]\text{O}_4$  samples synthesized at various temperatures when cycled between 2 and 5 V at  $10 \text{ mA g}^{-1}$ : (a)  $x = 0$ , (b)  $x = 0.25$ , (c)  $x = 0.5$ , (d)  $x = 0.75$ , and (e)  $x = 1$ .

spinel phase in the composite samples gradually increases with increasing synthesis temperature as seen in the  $x = 0$  composition due to both the (i) decreased solubility of Ni and the increased amount of  $\text{Mn}^{3+}$  in the spinel phase [28] and (ii) decreased degree of transition metal ordering in the spinel phase [32]. Similar to that found with the  $x = 1$  composition, the synthesis temperature does not clearly affect the lattice parameter of the layered phase in the composite samples.

For the  $x = 0.5$  composite samples synthesized at 700 and 900 °C, XRD and ND joint Rietveld refinement are performed to investigate the effect of the synthesis temperature on the composition and weight percentage changes of the layered and spinel phases. BET data are also measured with all the  $x = 0.5$  composite samples to investigate the surface area change with the synthesis

temperature. The obtained variations of the composition, weight percent, and surface area are given in Table 4. As seen in Table 4, a decrease in synthesis temperature leads to a slight ( $\sim 6$  wt. %) increase in the amount of the layered phase at the expense of the spinel phase. The weight percent of the cubic impurity phase is  $\sim 7$  wt. % regardless of the synthesis temperature. The refined compositions of the  $x = 0.5$  composite samples do not show abrupt compositional variations with the synthesis temperature. From this analysis, it is confirmed that synthesis temperatures between 700 and 900 °C do not severely affect the phase composition of the composite cathode with  $x = 0.5$ . Alternatively, the synthesis temperature clearly does affect the surface area of the composite cathode material. As we can see in Table 4, the surface area of the composite cathode material decreases significantly from 2.77 to

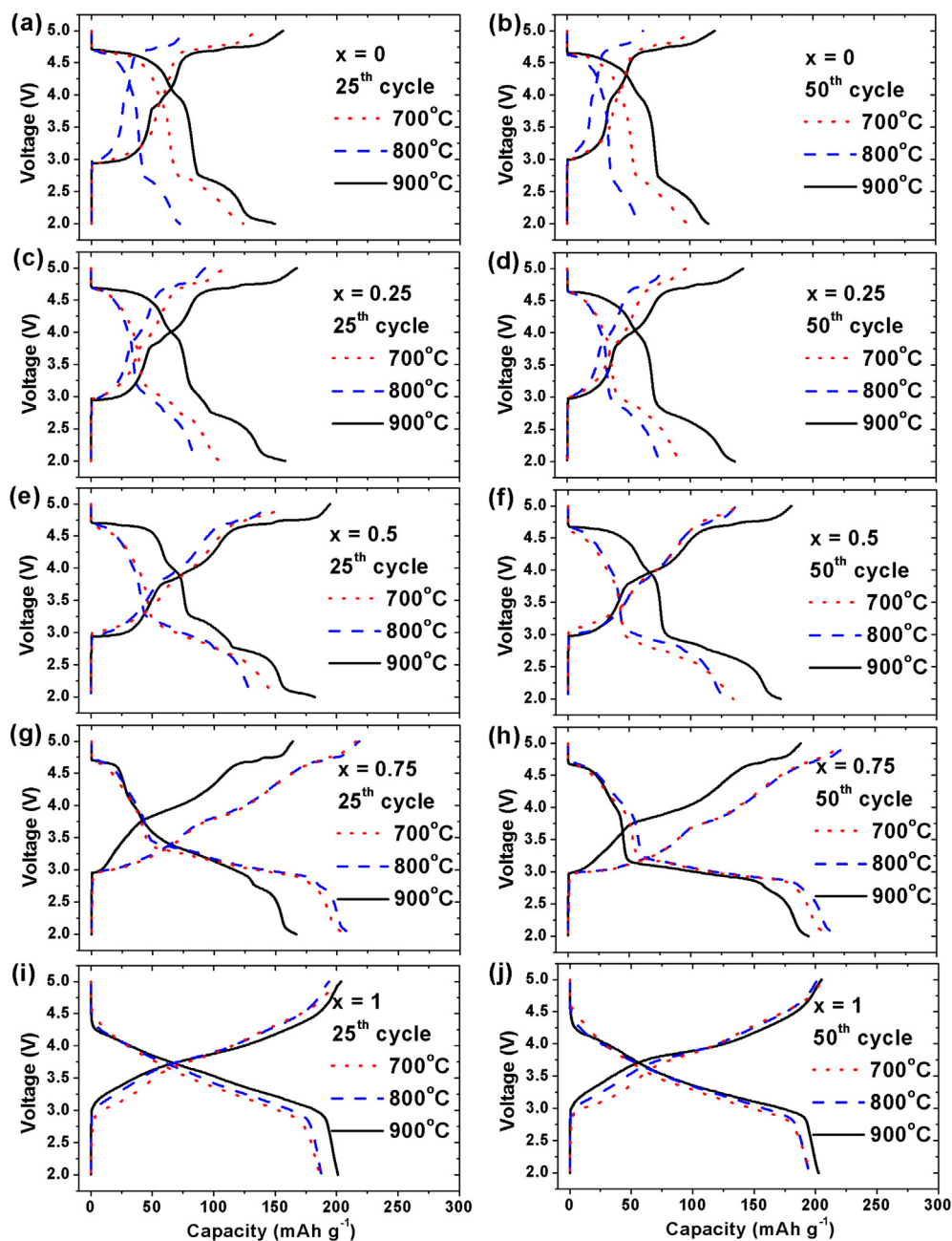


**Fig. 7.** Charge–discharge profiles of the  $x\text{Li}[\text{Li}_{0.2}\text{Mn}_{0.6}\text{Ni}_{0.2}]\text{O}_2-(1-x)\text{Li}[\text{Mn}_{1.5}\text{Ni}_{0.5}]\text{O}_4$  samples synthesized at various temperatures when cycled between 2 and 5 V at  $10\text{ mA g}^{-1}$ ; at the 25th cycle [(a)  $x = 0$ , (c)  $x = 0.25$ , (e)  $x = 0.5$ , (g)  $x = 0.75$ , and (i)  $x = 1$ ] and at the 50th cycle [(b)  $x = 0$ , (d)  $x = 0.25$ , (f)  $x = 0.5$ , (h)  $x = 0.75$ , and (j)  $x = 1$ ].

$0.03 \text{ m}^2 \text{ g}^{-1}$  as the synthesis temperature increases from 700 to 900 °C.

### 3.2. Electrochemistry

#### 3.2.1. First cycle charge–discharge profiles

Fig. 5 shows the first cycle charge–discharge profiles of the  $x\text{Li}[\text{Li}_{0.2}\text{Mn}_{0.6}\text{Ni}_{0.2}]\text{O}_2-(1-x)\text{Li}[\text{Mn}_{1.5}\text{Ni}_{0.5}]\text{O}_4$  ( $x = 0, 0.25, 0.5, 0.75$ , and 1) composite materials synthesized at different temperature. As reported previously, five distinctive plateaus are apparent during the discharge of the spinel  $\text{Li}[\text{Mn}_{1.5}\text{Ni}_{0.5}]\text{O}_4$  ( $x = 0$ ) phase [15,32]. The three plateaus above 3 V (two at  $\sim 4.7$  V and one at  $\sim 4.0$  V) are attributed to lithium ion insertion into the 8a tetrahedral sites of the cubic spinel structure. The two plateaus at  $\sim 4.7$  V are associated with the reduction of  $\text{Ni}^{4+}$  to  $\text{Ni}^{2+}$  through  $\text{Ni}^{3+}$  [31,36], while the  $\sim 4.0$  V plateau originates from the reduction of  $\text{Mn}^{4+}$  due to the existence of small amount of  $\text{Mn}^{3+}$  ions in the pristine state [8,24]. The plateau length at  $\sim 4.0$  V decreases with decreasing synthesis temperature due to the decrease in  $\text{Mn}^{3+}$  content in the spinel phase. The two plateaus below 3 V, at  $\sim 2.7$  and  $\sim 2.1$  V, originate from lithium-ion insertion into the empty 16c octahedral sites of the cubic spinel structure through the reduction of  $\text{Mn}^{4+}$  to  $\text{Mn}^{3+}$ , which is associated with a cubic to tetragonal phase transition [27,32,37–39]. As we can see in Fig. 5(a), the synthesis temperature affects the discharge profile below 3 V more significantly than above 3 V in the spinel phase. Recently, we have identified that the  $\sim 2.7$  and  $\sim 2.1$  V plateaus are accompanied by the creation of two different tetragonal phases with different lattice volumes and  $c/a$  ratios [32]. It appears that as the degree of transition metal ordering in the spinel phase increases, the capacity at the  $\sim 2.7$  V plateau increases at the expense of the capacity at the  $\sim 2.1$  V plateau [32]. The longer length of the  $\sim 2.7$  V plateau displayed by the ordered spinel sample is attributed to the facile lithium-ion insertion into the empty octahedral sites, with little lattice distortion as the empty octahedral sites (4a sites) in the ordered spinel are larger than the size of  $\text{Li}^+$  ions. On the other hand, the longer length of the  $\sim 2.1$  V plateau displayed by the disordered spinel sample is attributed to the sluggish lithium-ion insertion into the empty octahedral sites, with a large lattice distortion as the empty octahedral sites (16c sites) in the disordered spinel are smaller than the size of  $\text{Li}^+$  ions. In this regard, the increase in transition metal ordering in the 16d sites of the spinel phase with decreasing synthesis temperature is also confirmed by the electrochemical data, i.e. by the differences in the relative lengths of the plateaus at  $\sim 2.7$  and  $\sim 2.1$  V. In addition to the discharge capacities from the five spinel plateaus, a small capacity from the layered phase can also be observed as a sloping profile from 3.8 to 2.8 V for the sample synthesized at 700 °C, which is consistent with the XRD data in Fig. 3(a).

The lithium-rich layered oxide only composition  $\text{Li}[\text{Li}_{0.2}\text{Mn}_{0.6}\text{Ni}_{0.2}]\text{O}_2$  ( $x = 1$ ) shows the typical first charge and discharge profiles as expected from the literature [6,40]. The capacities of the sloping region (OCV to  $\sim 4.5$  V) during first charge, in which lithium-ion removal is associated with the oxidation of  $\text{Ni}^{2+}$  to  $\text{Ni}^{4+}$ , are similar regardless of the synthesis temperature [41,42]; however, the capacities of the plateau region (around 4.5 V) [6,43,44], which originate from the lithium-ion removal from the lattice by the oxidation of  $\text{O}^{2-}$  ions to O, decrease with decreasing synthesis temperature. This leads to a decrease in the first discharge capacity with decreasing synthesis temperature since the discharge capacity of lithium-rich layered oxides depends on the irreversible loss of oxygen from the lattice during the first charge [6]. This decrease in the plateau region with decreasing synthesis temperature could be due to the presence of more lithium ions in the transition metal layer, which originates from the increase in the

secondary spinel phase in the sample as mentioned earlier. As we reported before [15,40], the higher lithium content in the transition metal layer markedly affects lithium-ion extraction during the charge process due to the increased migration of nickel ions to the lithium layer [45]. The increased nickel ion content in the lithium layer decreases the lithium-ion diffusivity by interfering with the diffusion paths of lithium ions.

The composite materials  $x\text{Li}[\text{Li}_{0.2}\text{Mn}_{0.6}\text{Ni}_{0.2}]\text{O}_2-(1-x)\text{Li}[\text{Mn}_{1.5}\text{Ni}_{0.5}]\text{O}_4$  with  $x = 0.25, 0.5$ , and 0.75 show both the spinel and layered oxide characteristics in their charge–discharge profiles, as expected. Generally, the capacities from the spinel phase do not change much with synthesis temperature variation; however, it is noted that the capacity from the  $\sim 2.7$  V plateau increases at the expense of the  $\sim 2.1$  V plateau with decreasing synthesis temperature as is seen in the spinel only composition ( $x = 0$ ). In this regard, an increase in transition metal ordering in the spinel phase in the composite material is also expected with decreasing synthesis temperature, as in the spinel only ( $x = 0$ ) composition. Fig. 5(b)–(d) illustrates that the synthesis temperature noticeably affects the discharge capacity of the layered phase. This behavior is consistent with the previous studies on  $\text{Li}_2\text{MnO}_3$  [46]. The discharge capacity from the layered phase observed in the sloping region at 3.8–2.8 V increases with decreasing synthesis temperature due to the increase in the surface area of the samples as shown by the BET data in Table 4. The layered phases in the composite materials show smaller capacities than expected from the nominal composition, while the spinel phases show slightly higher capacities than expected from the nominal composition. This is due to the higher lithium-ion content in the transition metal layer of the layered phase as reported previously [15]. As we can see in Table 2, the actual lithium contents in the layered phases in the  $x = 0.25, 0.5$  and 0.75 samples synthesized at 800 °C are much higher than the nominal values. The higher capacities of the spinel phase in the composite materials are attributed to the higher weight percentages of the spinel phase than the nominal value, as we can see in Tables 2 and 4.

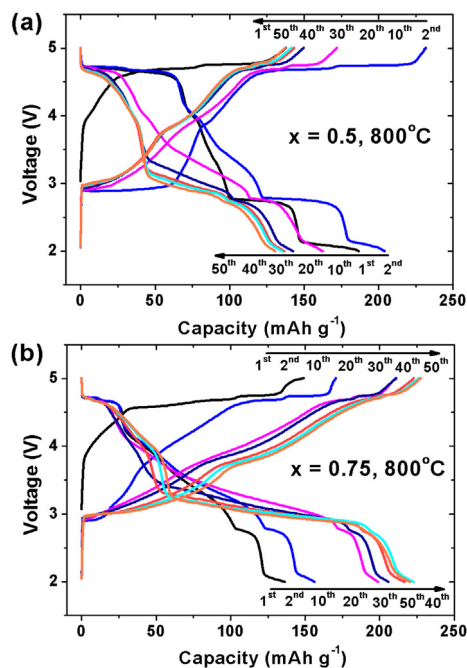


Fig. 8. Charge–discharge profiles of the 1st, 2nd, 10th, 20th, 30th, 40th and 50th cycles of the  $x\text{Li}[\text{Li}_{0.2}\text{Mn}_{0.6}\text{Ni}_{0.2}]\text{O}_2-(1-x)\text{Li}[\text{Mn}_{1.5}\text{Ni}_{0.5}]\text{O}_4$  samples synthesized at 800 °C when cycled between 2 and 5 V at  $10 \text{ mA g}^{-1}$ : (a)  $x = 0.5$  and (b)  $x = 0.75$ .



### 3.2.2. Cycle performance

Fig. 6 shows the cycle performances of the  $x\text{Li}[\text{Li}_{0.2}\text{Mn}_{0.6}\text{Ni}_{0.2}]\text{O}_2 - (1-x)\text{Li}[\text{Mn}_{1.5}\text{Ni}_{0.5}]\text{O}_4$  ( $x = 0, 0.25, 0.5, 0.75$ , and  $1$ ) composite materials synthesized at different temperatures. As reported before, the spinel  $\text{Li}[\text{Mn}_{1.5}\text{Ni}_{0.5}]\text{O}_4$  ( $x = 0$ ) samples show inferior cycle performance due to the large volume and  $c/a$  ratio changes which are attributed to the cubic to tetragonal phase transitions during lithium-ion insertion/extraction into/from the 16c octahedral sites [15,32]. On the other hand, the layered  $\text{Li}[\text{Li}_{0.2}\text{Mn}_{0.6}\text{Ni}_{0.2}]\text{O}_2$  ( $x = 1$ ) samples show good cycle performance. Interestingly, the layered samples synthesized at 700 and 800 °C show a gradual increase in discharge capacity over 50 cycles. After 50 cycles, all of the layered  $\text{Li}[\text{Li}_{0.2}\text{Mn}_{0.6}\text{Ni}_{0.2}]\text{O}_2$  samples display a similar discharge

capacity of about  $200 \text{ mAh g}^{-1}$ . The  $x = 0.25$  samples show inferior cycle performance similar to the  $x = 0$  sample due to the large fraction of the spinel phase in the samples. Unlike the cobalt-doped samples [15], the  $x = 0.5$  samples in this system also show inferior cycle performance except for the sample synthesized at 900 °C. The  $x = 0.75$  samples, however, exhibit a superior cycle performance with a gradual increase in discharge capacity over 50 cycles with characteristics similar to the cobalt-doped samples [15]. After 50 cycles, the discharge capacities of the  $x = 0.75$  samples reaches 213, 220, and 196  $\text{mAh g}^{-1}$ , respectively, for the 700, 800, and 900 °C samples. The reason for the varying cycle performance will be discussed in the following section with the charge–discharge profile analysis.

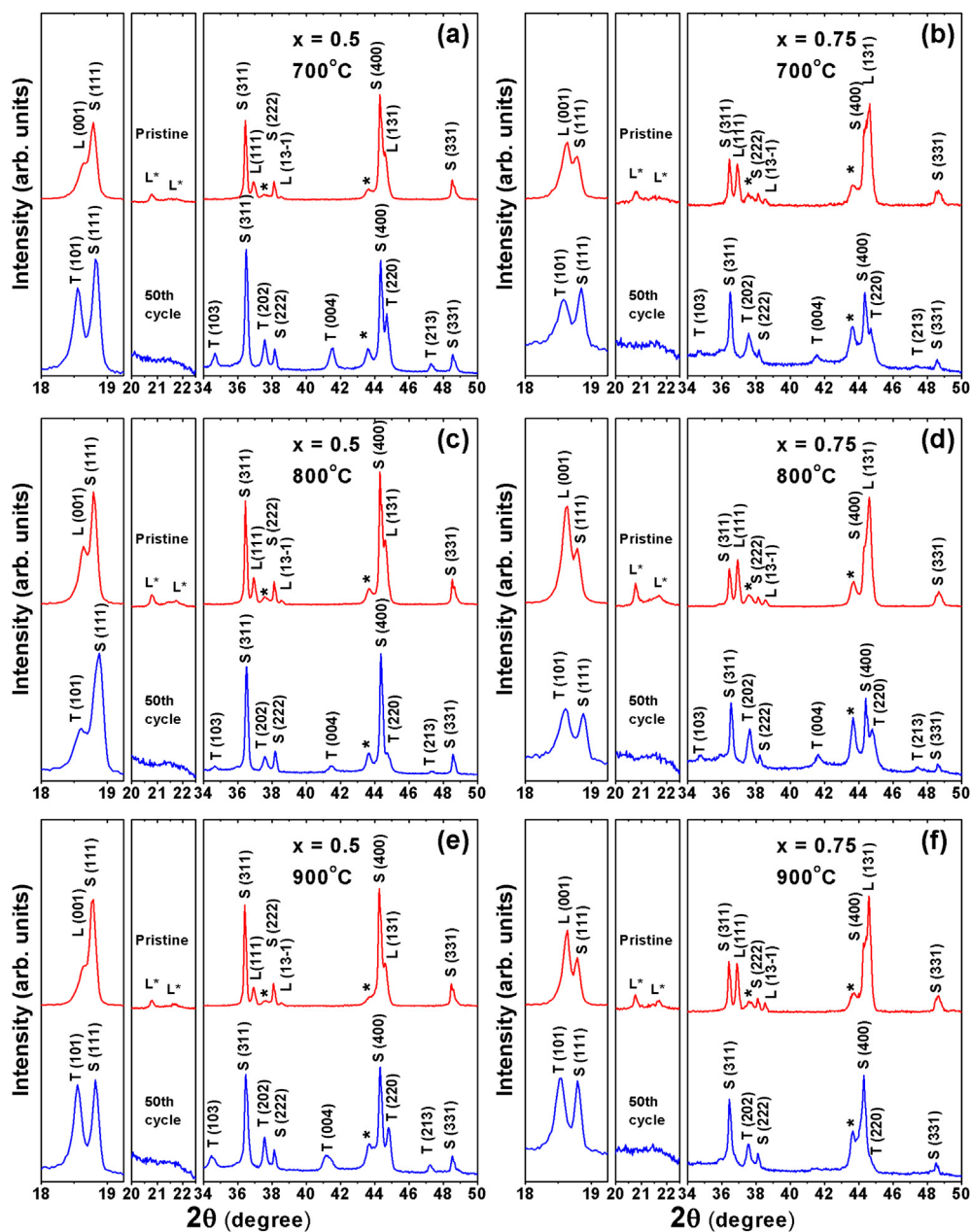


**Fig. 9.** Comparison of XRD patterns of the  $x\text{Li}[\text{Li}_{0.2}\text{Mn}_{0.6}\text{Ni}_{0.2}]\text{O}_2 - (1-x)\text{Li}[\text{Mn}_{1.5}\text{Ni}_{0.5}]\text{O}_4$  ( $x = 0.5$  and  $0.75$ ) samples synthesized at various temperatures before cycling and after the 50th cycle: (a)  $x = 0.5$  sample synthesized at 700 °C, (b)  $x = 0.75$  sample synthesized at 700 °C, (c)  $x = 0.5$  sample synthesized at 800 °C, (d)  $x = 0.75$  sample synthesized at 800 °C, (e)  $x = 0.5$  sample synthesized at 900 °C, and (f)  $x = 0.75$  sample synthesized at 900 °C. L, S, and T refer, respectively, to the layered, cubic spinel, and tetragonal spinel phases. L\* refers to the superstructure reflections arising from an ordering among the  $\text{Li}^+$ ,  $\text{Mn}^{4+}$ , and  $\text{Ni}^{2+}$  ions in the layered phase. The asterisk refers to the  $\text{NiMn}_2\text{O}_4$  cubic impurity phase.

### 3.2.3. Charge–discharge profile analysis during cycling

Fig. 7 compares the charge–discharge profiles at the 25th and 50th cycles of the  $x\text{Li}[\text{Li}_{0.2}\text{Mn}_{0.6}\text{Ni}_{0.2}]\text{O}_2-(1-x)\text{Li}[\text{Mn}_{1.5}\text{Ni}_{0.5}]\text{O}_4$  ( $x = 0, 0.25, 0.5, 0.75$ , and  $1$ ) composite materials synthesized at different temperatures. The spinel  $\text{Li}[\text{Mn}_{1.5}\text{Ni}_{0.5}]\text{O}_4$  ( $x = 0$ ) samples steadily lose their capacities as shown by the decreased length of the five distinctive plateaus during cycling. The sample synthesized at  $900^\circ\text{C}$  shows the lowest capacity reduction due to the decrease in the reaction of the cathode surface with the electrolyte caused by the smaller surface area. The layered  $\text{Li}[\text{Li}_{0.2}\text{Mn}_{0.6}\text{Ni}_{0.2}]\text{O}_2$  ( $x = 1$ ) samples show a gradual voltage decay even while delivering a constant discharge capacity for the  $900^\circ\text{C}$  sample and a steadily increasing discharge capacity for the  $800$  and  $700^\circ\text{C}$  samples. As reported in the literature, this voltage decay is explained by the slow phase transformation to a spinel-like phase during cycling by the migration of manganese and nickel ions into the lithium layer [15,45,47]. The  $x = 0.25$  samples show charge–discharge profile changes during 50 cycles similar to the  $x = 0$  sample due to the large fraction of the spinel phase in the samples. In addition to the capacity fade of the five distinctive plateaus, the capacity of the layered phase shown by the sloping region between  $3.8$  and  $2.8$  V at the first cycle in Fig. 5(b) also disappears by the 50th cycle.

The  $x = 0.5$  and  $0.75$  samples show similar charge–discharge profile changes over 50 cycles. As a representative example, several charge–discharge profiles of the  $x = 0.5$  and  $0.75$  samples synthesized at  $800^\circ\text{C}$  are shown in Fig. 8 to illustrate the details of the changes. The layered phases in the  $x = 0.5$  and  $0.75$  samples exhibit similar charge–discharge profile changes over 50 cycles. Initially, the discharge capacity in the sloping region ( $3.8$ – $2.8$  V) steadily increases due to the increased utilization of the layered phase, but then the gradient of the sloping region gradually decreases and finally changes to the  $\sim 3$  V plateau by the 50th cycle. We reported that this voltage profile change of the layered phase in the composite cathode materials originates from the gradual phase transformation of the layered phase to a  $3$  V spinel-like phase [15]. It is proposed that the newly created  $3$  V spinel-like phase does not suffer from Jahn–Teller distortion or Mn dissolution as the Mn oxidation state remains  $4+$  during the charge–discharge process [15]. On the other hand, the parent  $5$  V spinel phases in the  $x = 0.5$  and  $0.75$  samples gradually lose their capacity over 50 cycles. This is a different characteristic compared to our previous report on the cobalt-doped composite samples [15]. We believe that the relatively higher discharge capacity of the parent  $5$  V spinel phases at the  $\sim 2.7$  and  $\sim 2.1$  V plateaus in this system is the reason for the capacity fade of the parent  $5$  V spinel phase. In other words, a larger portion of the parent  $5$  V spinel phase undergoes Jahn–Teller distortion (cubic to tetragonal transformation) in this system compared to the system containing cobalt due to the smaller lattice distortion during lithium-ion insertion into the  $16d$  octahedral sites. From the aforementioned charge–discharge profile analysis, we deduce that the superior cycle performance of the  $x = 0.75$  samples originate from the higher wt. % of layered phase which undergoes a continuously increasing electrochemical utilization during cycling, followed by gradual phase transformation to a stable  $3$  V spinel-like phase.

### 3.2.4. Ex-situ XRD data analysis

We report that the layered phase in cobalt-doped layered-spinel composite materials ( $x = 0.5$  and  $0.75$ ) undergo complete phase transformation to a  $3$  V spinel-like phase after 50 cycles due to a higher lithium-ion content in the transition metal layer than the nominal composition [15]. It appears from the charge–discharge profile analyses that phase transformation of the layered phases in the  $x = 0.5$  and  $0.75$  samples also occur in this layered-spinel composite system. In order to confirm that the same phase

transformation phenomena can be found in this layered-spinel composite system regardless of synthesis temperature, *ex situ* XRD data are collected after the 50th cycle for all the  $x = 0.5$  and  $0.75$  composite samples in the discharged state. The *ex situ* XRD data after 50 cycles are compared with the pristine XRD data in Fig. 9. As we can see in Fig. 9, after the 50th cycle, the reflections corresponding to the layered phase ( $C2/m$ ), such as the  $(001)$ ,  $(111)$ , and  $(131)$  reflections, completely vanish in all the  $x = 0.5$  and  $0.75$  samples irrespective of their synthesis temperature. Instead of the reflections corresponding to the layered phase ( $C2/m$ ), the reflections corresponding to the tetragonal phase ( $I4_1/amd$ ) are observed in addition to the reflections corresponding to the cubic spinel phase ( $Fd-3m$ ), which is similar to the results found in our previous report [15]. The tetragonal phase ( $I4_1/amd$ ) originates from the cubic to tetragonal phase transition of the parent  $5$  V spinel phase during discharge down to  $2$  V. By combining the *ex situ* XRD data after the 50th cycle and the formation of a  $3$  V plateau at the 50th cycle in the charge–discharge profile analysis data in Fig. 7f and h, we can also confirm the complete transformation of the layered phase ( $C2/m$ ) in the  $x = 0.5$  and  $0.75$  samples to a  $3$  V spinel-like phase ( $Fd-3m$ ) after 50 cycles similar to that in our previous report [15].

## 4. Conclusions

The effect of synthesis temperature on the structural and electrochemical characteristics of the layered-spinel composite system  $x\text{Li}[\text{Li}_{0.2}\text{Mn}_{0.6}\text{Ni}_{0.2}]\text{O}_2-(1-x)\text{Li}[\text{Mn}_{1.5}\text{Ni}_{0.5}]\text{O}_4$  ( $0 \leq x \leq 1$ ) has been investigated systematically with XRD, ND, and electrochemical measurements. By joint ND and XRD Rietveld refinement method, the composition and weight percentage variations of the layered and spinel phases in the composite samples with different synthesis temperatures have been obtained. While no pronounced composition and weight percentage variations are found with the synthesis temperature, the electrochemical characteristics of both the layered and spinel phases are highly affected by the synthesis temperature. The capacity from the layered phase increases with decreasing synthesis temperature due to the increased surface area. For the spinel phase, synthesis temperature highly affects the discharge profile below  $3$  V due to the decrease in lattice distortion by the increase in the transition metal ordering with decreasing synthesis temperature. The combined electrochemical and *ex situ* XRD data reveal a complete transformation of the layered phase ( $C2/m$ ) in the  $x = 0.5$  and  $0.75$  samples to a  $3$  V spinel-like phase ( $Fd-3m$ ) after 50 cycles due to the higher lithium-ion content in the layered phase, which is similar to that found previously with the cobalt-doped systems [15]. In contrast to cobalt-doped systems [15], the parent  $5$  V spinel phases in the  $x = 0.5$  and  $0.75$  samples gradually lose their capacity over 50 cycles due to the higher capacity of the  $\sim 2.7$  and  $2.1$  V plateaus, which is associated with a cubic to tetragonal phase transition involving large volume and  $c/a$  ratio changes. The study suggests that tailored and optimized electrochemical characteristics of layered-spinel composite cathode materials could be possible by controlling the transition metal composition, synthesis temperature, transition metal ordering in the spinel phase, and the particle size of the samples.

## Acknowledgments

This work was supported by the U.S. Department of Energy, Office of Basic Energy Sciences, Division of Materials Sciences and Engineering under award number DE-SC0005397. Neutron diffraction portion of this research at ORNL's Spallation Neutron Source was sponsored by the Scientific User Facilities Division, Office of Basic Energy Sciences, U.S. Department of Energy.

## Appendix A. Supplementary data

Supplementary data related to this article can be found at <http://dx.doi.org/10.1016/j.jpowsour.2013.04.010>.

## References

- [1] M. Armand, J.-M. Tarascon, *Nature* 451 (2008) 652–657.
- [2] M.M. Thackeray, C. Wolverton, E.D. Isaacs, *Energy Environ. Sci.* 5 (2012) 7854–7863.
- [3] A. Manthiram, *J. Phys. Chem. Lett.* 2 (2011) 176–184.
- [4] Z. Lu, D.D. MacNeil, J.R. Dahn, *Electrochem. Solid-State Lett.* 4 (2001) A191–A194.
- [5] C.S. Johnson, N. Li, C. Lefief, M.M. Thackeray, *Electrochem. Commun.* 9 (2007) 787–795.
- [6] A.R. Armstrong, S.-H. Kang, M. Holzapfel, P. Nova, M.M. Thackeray, P.G. Bruce, *J. Am. Chem. Soc.* 128 (2006) 8694–8698.
- [7] K. Amine, H. Tukamoto, H. Yasuda, Y. Fuiita, *J. Electrochem. Soc.* 143 (1996) 1607–1613.
- [8] Q. Zhong, A. Bonakclarpour, M. Zhang, J.R. Dahn, *J. Electrochem. Soc.* 144 (1997) 205–213.
- [9] C.S. Johnson, N. Li, J. Vaughey, S. Hackney, M.M. Thackeray, *Electrochem. Commun.* 7 (2005) 528–536.
- [10] J. Cabana, C.S. Johnson, X.Q. Yang, K.Y. Chung, W.-S. Yoon, S.H. Kang, M.M. Thackeray, C.P. Grey, *J. Mater. Res.* 25 (2010) 1601–1616.
- [11] S. Park, S.H. Kang, C.S. Johnson, K. Amine, M.M. Thackeray, *Electrochem. Commun.* 9 (2007) 262–268.
- [12] J. Cabana, S.H. Kang, C.S. Johnson, C.P. Grey, M.M. Thackeray, *J. Electrochem. Soc.* 156 (2009) A730–A736.
- [13] H. Deng, I. Belharouak, Y.-K. Sun, K. Amine, *J. Mater. Chem.* 19 (2009) 4510–4516.
- [14] H. Deng, I. Belharouak, R.E. Cook, H. Wu, Y.-k. Sun, K. Amine, *J. Electrochem. Soc.* 157 (2010) A447–A452.
- [15] E.-S. Lee, A. Huq, H.-Y. Chang, A. Manthiram, *Chem. Mater.* 24 (2012) 600–612.
- [16] A. Huq, J.P. Hodges, O. Gourdon, L. Heroux, Z. Kristallogr. Proc. 1 (2011) 127.
- [17] A.C. Larson, R.B.V. Dreele, in: *Los Alamos National Laboratory Report LAUR*, Los Alamos National Laboratory, Los Alamos, NM, USA, 2000, p. 86.
- [18] B.H. Toby, *J. Appl. Crystallogr.* 34 (2001) 210–213.
- [19] G. Schuck, A. Iwata, A. Sasaki, A. Himeda, H. Konaka, N. Muroyama, *Acta Crystallogr. Sect. A* A66 (2010) S311.
- [20] Y.S. Meng, G. Ceder, C.P. Grey, W.-S. Yoon, M. Jiang, J. Breger, *Chem. Mater.* 2 (2005) 2386–2394.
- [21] C.R. Fell, K.J. Carroll, M. Chi, Y.S. Meng, *J. Electrochem. Soc.* 157 (2010) A1202–A1211.
- [22] K. Amine, H. Tukamoto, H. Yasuda, Y. Fujita, *J. Power Sources* 68 (1997) 604–608.
- [23] H. Taguchi, S. Omori, M. Nagao, H. Kido, M. Shimada, *J. Solid State Chem.* 118 (1995) 112–116.
- [24] M. Kunduraci, G.G. Amatucci, *J. Electrochem. Soc.* 153 (2006) A1345–A1352.
- [25] M. Kunduraci, J.F. Al-Sharab, G.G. Amatucci, *Chem. Mater.* 18 (2006) 3585–3592.
- [26] J. Kim, S. Myung, C.S. Yoon, S.G. Kang, Y. Sun, *Chem. Mater.* 16 (2004) 906–914.
- [27] K. Ariyoshi, Y. Iwakoshi, N. Nakayama, *J. Electrochem. Soc.* (2004) 296–303.
- [28] D.W. Shin, C.A. Bridges, A. Huq, M.P. Paranthaman, A. Manthiram, *Chem. Mater.* 24 (2012) 3720–3731.
- [29] S.-T. Myung, S. Komaba, N. Kumagai, H. Yashiro, H.-T. Chung, T.-H. Cho, *Electrochim. Acta* 47 (2002) 2543–2549.
- [30] P. Strobel, A. Ibarra-Palos, M. Anne, C. Poinssignon, A. Crisci, *Solid State Sci.* 5 (2003) 1009–1018.
- [31] M. Kunduraci, G.G. Amatucci, *J. Power Sources* 165 (2007) 359–367.
- [32] E.-S. Lee, K.-W. Nam, E. Hu, A. Manthiram, *Chem. Mater.* 24 (2012) 3610–3620.
- [33] Y. Idemoto, H. Narai, N. Koura, *J. Power Sources* 119 (2003) 125–129.
- [34] Y. Idemoto, H. Sekine, K. Ui, N. Koura, *Solid State Ionics* 176 (2005) 299–306.
- [35] K.A. Jarvis, Z. Deng, L.F. Allard, A. Manthiram, P.J. Ferreira, *Chem. Mater.* (2011) 3614–3621.
- [36] Y. Terada, K. Yasaka, F. Nishikawa, T. Konishi, M. Yoshio, I. Nakai, *J. Solid State Chem.* 156 (2001) 286–291.
- [37] M.M. Thackeray, *Prog. Solid State Chem.* 25 (1997) 1–71.
- [38] S.H. Park, S.-W. Oh, C.-S. Yoon, S.-T. Myung, Y.-K. Sun, *Electrochem. Solid-State Lett.* 8 (2005) A163–A167.
- [39] S. Park, S. Oh, S.H. Kang, I. Belharouak, K. Amine, Y. Sun, *Electrochim. Acta* 52 (2007) 7226–7230.
- [40] T.A. Arunkumar, Y. Wu, A. Manthiram, *Chem. Mater.* 19 (2007) 3067–3073.
- [41] X.-Q. Yang, J. McBreen, W.-S. Yoon, C.P. Grey, *Electrochem. Commun.* 4 (2002) 649–654.
- [42] J. Breger, Y.S. Meng, Y. Hinuma, S. Kumar, K. Kang, *Chem. Mater.* 18 (2006) 4768–4781.
- [43] P. Kalyani, S. Chitra, T. Mohan, S. Gopukumar, *J. Power Sources* 80 (1999) 103–106.
- [44] A.D. Robertson, P.G. Bruce, *Chem. Mater.* 15 (2003) 1984–1992.
- [45] B. Xu, C.R. Fell, M. Chi, Y.S. Meng, *Energy Environ. Sci.* 4 (2011) 2223–2233.
- [46] D.Y.W. Yu, K. Yanagida, Y. Kato, H. Nakamura, *J. Electrochem. Soc.* 156 (2009) A417–A424.
- [47] J.R. Croy, D. Kim, M. Balasubramanian, K. Gallagher, S.-H. Kang, M.M. Thackeray, *J. Electrochem. Soc.* 159 (2012) A781–A790.